Biomicrofluidics 19, 024104 (2025); published version at https://doi.org/10.1063/5.0263344

Mechanical interaction between a hydrogel and an embedded cell in biomicrofluidic applications

Lei Li[1], Jiaqi Zhang[2,3], Pengtao Yue[4], and James J. Feng*[1,5]

[1]Department of Chemical and Biological Engineering, University of British Columbia, Vancouver, BC V6T 1Z3, Canada
[2]Research Center for Mathematics, Advanced Institute of Natural Sciences, Beijing Normal University, Zhuhai, 519087, China
[3]Guangdong Provincial/Zhuhai Key Laboratory of IRADS, BNU-HKBU United International College, Zhuhai 519087, China
[4]Department of Mathematics, Virginia Tech, Blacksburg, VA 24061, USA
[5]Department of Mathematics, University of British Columbia, Vancouver, BC V6T 1Z2, Canada

Abstract

Thanks to their softness, biocompatibility, porosity and ready availability, hydrogels are commonly used in microfluidic assays and organ-on-chip devices as a matrix for cells. They not only provide a supporting scaffold for the differentiating cells and the developing organoids, but also serve as the medium for transmitting oxygen, nutrients, various chemical factors, and mechanical stimuli to the cells. From a bioengineering viewpoint, the transmission of forces from fluid perfusion to the cells through the hydrogel is critical to the proper function and development of the cell colony. In this paper, we develop a poroelastic model to represent the fluid flow through a hydrogel containing a biological cell modeled as a hyperelastic inclusion. In geometries representing shear and normal flows that occur frequently in microfluidic experiments, we use finite-element simulations to examine how the perfusion engenders interstitial flow in the gel and displaces and deforms the embedded cell. Results show that the pressure is the most important stress component in moving and deforming the cell, and the model predicts velocity in the gel and stress transmitted to the cell that are comparable to *in vitro* and *in vivo* data. This work provides a computational tool to design the geometry and flow conditions to achieve optimal flow and stress fields inside the hydrogels and around the cell.

*Corresponding author, james.feng@ubc.ca

1 Introduction

Hydrogels are soft materials consisting of a crosslinked polymer network swollen with an aqueous solvent. The solid network typically amounts to only a few percent in volume or weight, thus rendering the gel soft, porous and highly permeable [1]. In addition, hydrogels are nontoxic and readily available, and their properties are easily tunable via the concentrations of the solid content and crosslinking. For those reasons, hydrogels are widely used to mimic the extracellular matrix (ECM) in *in vitro* cell cultures, disease models, and tissue engineering [2–8]. Moreover, hydrogels are finding new applications in encapsulating cells and drugs for processing and delivery [9–14].

In such applications, the hydrogel plays several roles. The most obvious is as physical support for the cells. An equally important role is as a medium through which nutrients and chemical signaling factors can be transported, via convection (interstitial flow), diffusion or a combination of both [15, 16]. Finally, the gel also serves as a medium for mechanotransduction [17, 18]. Shear and normal stresses are transmitted through the hydrogel to the cells, and such mechanical stimuli regulate a wide range of cell behaviors, including cytokinesis [19], differentiation of stem cells [17, 20], endothelial-to-mesenchymal transition [21], tumor cell proliferation [22], sprouting angiogenesis [23], epithelial mucus production [24] and T cell activation [25], among many others. However, excessive strain and stress in the hydrogel can induce cell death and extrusion [26, 27].

Clearly, it will be desirable to know the interstitial flow and the strain and stress distributions in the hydrogel medium around the cells. So far, two modeling frameworks have been developed to describe the mechanics of hydrogels [28]. The monophasic approach treats the hydrogel as a single-phase elastic [29, 30] or viscoelastic material [31, 32]. The solvent and any dissolved species diffuse in this medium, but contribute nothing to the overall momentum balance. The multiphasic approach, on the other hand, views the interstitial fluid and the polymer network as two different phases, and explicitly accounts for the interstitial flow of the solvent [33–36]. The latter is more suitable for our purpose, because in biomicrofluidic and organ-on-chip devices, the hydrogel is typically in contact with a flowing liquid that perfuses the cell culture [5, 8, 14, 37]. The flow and transport across the fluid-hydrogel interface is a complex problem that has only recently begun to receive rigorous analysis in the fluid mechanics literature [38–40]. The interfacial transport is coupled with the gel deformation, the interstitial flow inside the gel, and the movement and deformation of the cells. Through

this string of coupled processes, the perfusing stream can impart a certain magnitude of flow around the cells, and transmitting a certain level of stress to them. Given the complexity of the problem, therefore, it is no surprise that there has been little quantitative understanding, control or optimization of these factors and processes in laboratory experiments.

Nevertheless, several groups have made important advances toward the above goal. Polacheck *et al.* [41] computed a pressure-driven normal flow through a porous layer using the Brinkman model, and estimated the flow and stresses around an embedded solid cylinder that represents an biological cell. Novak *et al.* [22] did similar computations for a shear-dominated flow with a spherical inclusion. Bachmann *et al.* [42] solved for the flow and diffusion in a gel-filled chamber sheared by perfusion, but treated the gel as a Newtonian fluid, without an explicit account of its porous nature nor the presence of embedded cells. These efforts have offered glimpses of the flow and stress fields inside the hydrogel surrounding the cells. But they have neglected certain key factors in the process, including the fluid-to-gel interfacial transport and the deformability of the gel and the cells. Several important questions remain open:

- How does a hydrogel deform when it is in contact with a flowing fluid? How much elastic strain and stress develop within the gel, and how are these distributed?
- Subject to the hydrogel deformation, how much fluid penetrates into the gel domain under a prescribed external pressure or flow rate, and how is the fluid velocity distributed inside the gel?
- How much flow, strain and stress does the gel transmit to an embedded cell? How much does the cell move and deform as a consequence?

We aim to tackle these questions systematically, first by building a modeling framework that properly accounts for the poroelastic mechanics of the hydrogels and the deformability of the embedded cells. Using finite elements, we then simulate the dynamics of the coupled fluid-hydrogel-cell system in geometries motivated by some of the successful experimental devices cited above. The numerical results are interrogated to provide answers to the open questions. Our model, computational tools and the new insights gathered here can be applied to the design and optimization of future biomicrofluidic and organ-on-chip devices based on hydrogels.

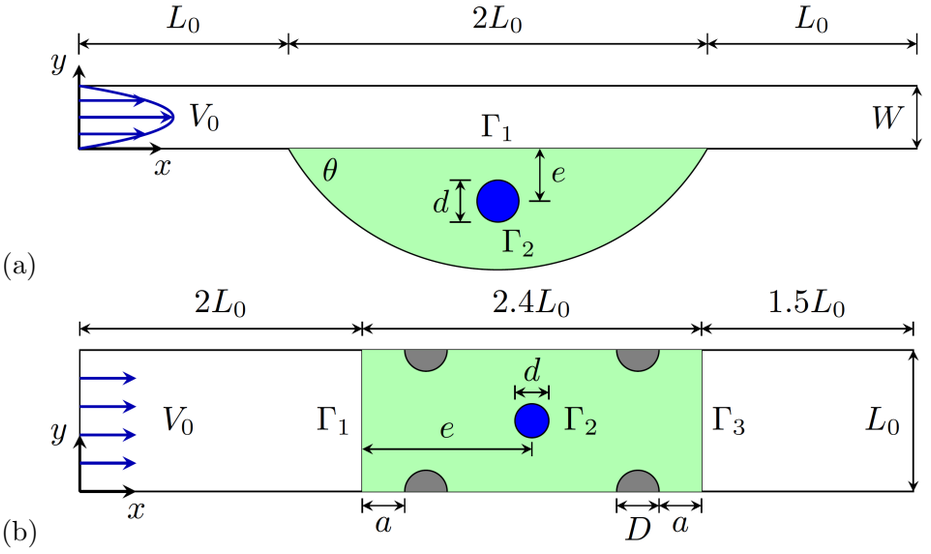

Figure 1: Geometric setup for our numerical simulations. (a) The shear flow geometry, based on the device of [42], features a channel flow of the perfusate passing by a sac-like gel domain containing an embedded cell. (b) The normal flow geometry, based on the device of [41], shows a gel layer held in place by solid posts (grey semi-circles). The solvent passes normally through the layer.

2 Problem setup and methodology

2.1 Geometry

We base the geometric setup of our simulations on two microfluidic devices in recent experiments. Bachmann *et al.* [42] have cultivated cells in a hydrogel chamber that is attached to the side of the perfusing channel. Thus, the flow direction in the channel is parallel to the fluid-gel interface, and the perfusate predominantly shears the gel surface. In Polacheck *et al.* [41], on the other hand, a gel layer separates two fluid channels at different pressures. The pressure drop drives a flow across the gel layer, which is mostly perpendicular to the gel surfaces. From these two applications, we have extracted the simplified two-dimensional (2D) geometries shown in Fig. 1. They are relatively simple, but capture the distinct features of interstitial flow and are realistic enough to bear on the questions of interest. They will be referred to, respectively, as the shear-flow and normal-flow geometries.

In the shear-flow geometry (Fig. 1a), the perfusate enters from the left of the channel with a fully developed parabolic velocity profile of maximum velocity V_0, and then passes alongside the fluid-gel interface Γ_1 to drive an interstitial flow inside the gel. The interstitial flow goes around a cell embedded in the gel, with the cell-gel interface denoted by Γ_2. There are multiple lengths in the geometric setup, which are marked in the diagram. We fix the channel and gel-chamber geometry with $W = 0.2L_0$ and $\theta = \pi/3$, and the cell's initial location at $e = 0.2L_0$. The cell diameter $d = 0.06L_0$ is fixed in both the shear- and normal-flow geometries.

In the normal-flow geometry (Fig. 1b), the gel layer extends up and down in the y-direction, and is held in place by the solid circular posts. The computational domain shown here is one repeating unit of the gel layer, with symmetry boundary conditions at the top ($y = L_0$) and bottom $y = 0$. The perfusate flows with uniform velocity V_0 normal to the gel layer, penetrates the upstream interface Γ_1, flows through the gel and exits the downstream interface Γ_3. A biological cell is embedded in the middle of the gel layer, with interface Γ_2. The overall geometry is fixed with the post diameter $D = 0.4L_0$, and clearance $a = 0.2L_0$. We will vary the cell position e to study how the location affects the cell deformation.

2.2 Governing equations

The theoretical model has two major components: a poroelastic description of the mechanics of the bulk of the gel, and a suitable set of boundary conditions on the interface between the gel and the solvent. The poroelastic governing equations are well-known from recent studies [35, 38], and so we only give a brief summary below.

The hydrogel is viewed as an effective continuum consisting of a solid network of volume fraction ϕ_s and a solvent of volume fraction $\phi_f = 1 - \phi_s$. Each phase has its own velocity and stress tensor, and its motion is governed by the continuity and momentum equations, with a Darcy drag term representing the momentum exchange between the two:

$$\frac{\partial \phi_s}{\partial t} + \nabla \cdot (\phi_s \mathbf{v}_s) = 0, \tag{1}$$

$$\nabla \cdot (\phi_s \mathbf{v}_s + \phi_f \mathbf{v}_f) = 0, \tag{2}$$

$$\nabla \cdot (\phi_f \boldsymbol{\sigma}_f) - \phi_f \nabla p + \xi \phi_f \phi_s (\mathbf{v}_s - \mathbf{v}_f) = 0, \tag{3}$$

$$\nabla \cdot (\phi_s \boldsymbol{\sigma}_s) - \phi_s \nabla p + \xi \phi_f \phi_s (\mathbf{v}_f - \mathbf{v}_s) = 0, \tag{4}$$

$$\frac{d\mathbf{u_s}}{dt} - \mathbf{v_s} = 0, \tag{5}$$

where $\mathbf{v}_f$ and $\mathbf{v}_s$ are the phase-averaged velocities of the fluid and solid phases, $\boldsymbol{\sigma}_f$ and $\boldsymbol{\sigma}_s$ are their Cauchy stress tensors, p is the shared pressure, and $\mathbf{u}_s$ is the displacement of the solid phase in the hydrogel. The Darcy drag is proportional to the relative velocity between the two phases, with ξ being a constant drag coefficient. Equation (1) describes the transport of the solid phase. A similar one can be written for the fluid phase, but in its place, we have used the sum of the two in Eq. (2).

For the interstitial fluid of viscosity μ, we have $\boldsymbol{\sigma}_f = \mu[\nabla \mathbf{v}_f + (\nabla \mathbf{v}_f)^T]$. For the solid network, we adopt the hyperelastic neo-Hookean model so as to allow large strains:

$$\boldsymbol{\sigma}_s = \mu_s J^{-1}(\mathbf{F} \cdot \mathbf{F}^T - \mathbf{I}) + \lambda_s (J-1)\mathbf{I}, \tag{6}$$

where $\mathbf{F}$ is the deformation gradient, $J = \det(\mathbf{F})$ is its determinant, $\mathbf{I}$ is the unit tensor, and λ_s and μ_s are the first and second Lamé parameters, which are related to Young's modulus E and Poisson's ratio ν as follows:

$$\lambda_s = \frac{E\nu}{(1+\nu)(1-2\nu)}, \quad \mu_s = \frac{E}{2(1+\nu)}. \tag{7}$$

The Green-Lagrangian strain tensor $\mathbf{E} = (\mathbf{F} \cdot \mathbf{F}^T - \mathbf{I})/2$ and its components will be used later to analyze the degree of deformation of the hydrogel and the embedded cells. Another way to represent the "overall strength" of a stress or strain tensor is by its second invariant. For the stress tensor $\boldsymbol{\sigma}_s$, in particular, we can define the von Mises stress as

$$\sigma_{sv} = \sqrt{\sigma_{sxx}^2 + \sigma_{syy}^2 - \sigma_{sxx}\sigma_{syy} + 3\sigma_{sxy}^2} \tag{8}$$

in 2D planar geometry. A von Mises strain can be similarly defined as a scalar representation of the intensity of solid deformation.

For the flow of the viscous solvent outside the gel, we neglect inertia and pose the Stokes equation for the exterior velocity $\mathbf{V}$ and the pressure P:

$$\nabla \cdot \mathbf{V} = 0, \tag{9}$$

$$\nabla \cdot \boldsymbol{\Sigma} - \nabla P = 0, \tag{10}$$

where $\boldsymbol{\Sigma} = \mu[\nabla \mathbf{V} + (\nabla \mathbf{V})^T]$ is the viscous stress tensor.

We model the embedded cell also as a neo-Hookean solid, but with different Lamé constants λ_c and μ_c. Depending on the cell types, they can have a wide range of stiffness, with Young's modulus ranging from hundreds

to thousands of pascals [43], comparable to that of hydrogels [44]. The deformation and movement of the cell are governed by

$$\nabla \cdot \boldsymbol{\sigma}_c = 0, \tag{11}$$

$$\frac{d\mathbf{u}_c}{dt} - \mathbf{v}_c = 0, \tag{12}$$

where $\boldsymbol{\sigma}_c$ is the Cauchy stress tensor, and $\mathbf{u}_c$ and $\mathbf{v}_c$ are the displacement and velocity fields in the cell, respectively. In presenting the results, we will also discuss the centroid movement of the cell.

As will be seen shortly, the elastic strains in the gel and the cell will be small under typical flow conditions in a microfluidic device. Therefore, the results would not change appreciably if we had adopted linear elasticity for the solid network and the cell. We have retained the neo-Hookean model for potential applications to large-strain conditions. The added complexity to the computation is minimal. As long as we have to track the solid deformation, using the Lagrangian coordinates is unavoidable, and computing the nonlinear strain requires little extra work.

2.3 Boundary conditions

Our flow geometries of Fig. 1 feature the fluid-gel interfaces Γ_1 and Γ_3, and the gel-cell interface Γ_2. On Γ_1 and Γ_3, we ignore interfacial tension and impose the following boundary conditions developed recently [38–40]:

$$(\mathbf{V} - \mathbf{v}_s) \cdot \mathbf{n} = \phi_f (\mathbf{v}_f - \mathbf{v}_s) \cdot \mathbf{n}, \tag{13}$$

$$(-p\mathbf{I} + \phi_f \boldsymbol{\sigma}_f + \phi_s \boldsymbol{\sigma}_s) \cdot \mathbf{n} = (-P\mathbf{I} + \boldsymbol{\Sigma}) \cdot \mathbf{n}, \tag{14}$$

$$(\mathbf{V} - \mathbf{v}_f) \cdot \mathbf{n} = \eta \mathbf{n} \cdot [(\boldsymbol{\Sigma} - P\mathbf{I}) - (\boldsymbol{\sigma}_s - p\mathbf{I})] \cdot \mathbf{n}, \tag{15}$$

$$(\mathbf{V} - \mathbf{v}_f) \cdot \mathbf{t} = \beta (\boldsymbol{\Sigma} \cdot \mathbf{n}) \cdot \mathbf{t}, \tag{16}$$

$$\phi_s (\mathbf{v}_s - \mathbf{v}_f) \cdot \mathbf{t} = -\beta (\boldsymbol{\sigma}_s \cdot \mathbf{n}) \cdot \mathbf{t}, \tag{17}$$

where $\mathbf{n}$ and $\mathbf{t}$ are the normal and tangent vectors to the gel surface, respectively, with $\mathbf{n}$ pointing outward from the gel toward the fluid. η is an interfacial permeability, and β is an interfacial slip coefficient. On Γ_2, the coupling between the hydrogel and the cell satisfies continuity of displacement, velocity and traction:

$$\mathbf{v}_s = \mathbf{v}_f = \mathbf{v}_c, \tag{18}$$

$$\mathbf{u}_s = \mathbf{u}_c, \tag{19}$$

$$\boldsymbol{\sigma}_c \cdot \mathbf{n} = (\phi_s \boldsymbol{\sigma}_s + \phi_f \boldsymbol{\sigma}_f - p\mathbf{I}) \cdot \mathbf{n}, \tag{20}$$

where $\mathbf{n}$ represents the normal vector to Γ_2.

In the shear-flow geometry (Fig. 1a), the fluid enters the 2D channel with a fully developed parabolic velocity profile of maximum velocity V_0. On the exit, we impose the zero-stress natural boundary condition. On the solid walls of the channel, we impose no-slip condition. On the circular boundary of the gel chamber, we impose no-slip for the interstitial fluid ($\mathbf{v}_f = \mathbf{0}$) and for the solid network ($\mathbf{u}_s = \mathbf{0}$). In the normal-flow geometry (Fig. 1b), the fluid has a uniform entry velocity V_0 upstream of the gel layer, and the zero-stress natural boundary condition at the exit on the right. On the surface of the solid posts, we again adopt $\mathbf{v}_f = \mathbf{0}$ and $\mathbf{u}_s = \mathbf{0}$. Because of symmetry, only the lower half of the domain will be computed. On the bottom ($y = 0$) and the midline ($y = 0.5L_0$) of the domain, symmetric conditions are used, with $\partial/\partial y = 0$.

We render the governing equations and boundary conditions dimensionless before solving them numerically. See Appendix A for details of the scaling. In presenting the results, we will mostly use dimensionless variables and parameters defined therein. Most of the model parameters can be estimated from typical material properties and experimental devices, and details can be found in Appendix B. Based on these, we have chosen the baseline set of dimensionless parameters in Table 1 of Appendix B. In the following, we first report numerical simulations that use these parameters, and then vary certain parameters as appropriate.

2.4 Numerical methods

The computations use the finite-element methods developed by Li *et al.* [35], where details can be found. In brief, we track the fluid-gel interface using a fixed-mesh arbitrary Lagrangian-Eulerian method. The interfacial deformation, the interstitial fluid flow and the solid displacement are solved together in a monolithic algorithm using the finite-element library deal.II [45]. To handle the complex geometry and larger scale of the simulations here, we have further extended the code of Li *et al.* [35] by implementing MPI-based parallel computing [46]. For solving the linear systems, the original serial direct solver UMFPACK [47] has been replaced by a parallel package, Trilinos MUMPs [48–50]. These have greatly improved the capacity and speed of the code.

A typical mesh is shown in Fig. 2 for the shear-flow geometry, with Q2 quadrilateral elements, each edge being resolved by 3 nodes. The flow around the embedded cell and the elastic deformation inside the cell require refinement in and around it, and the fine mesh is illustrated in the blowup

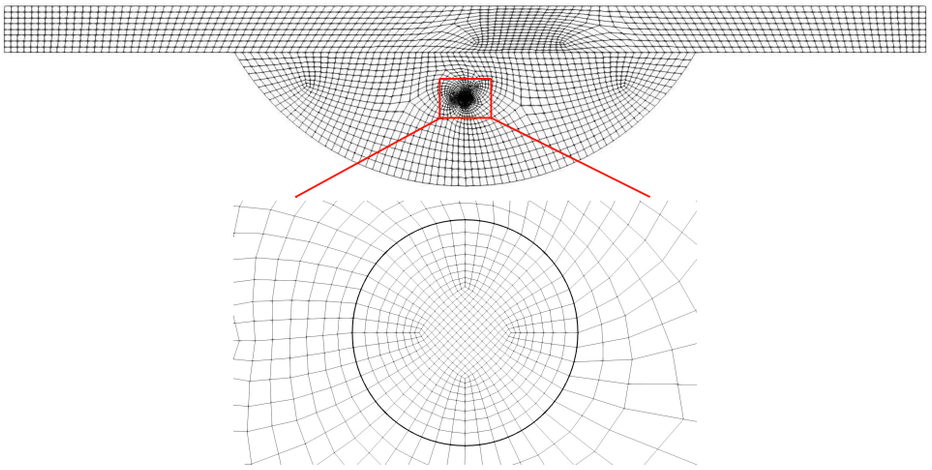

Figure 2: A typical mesh for the shear-flow geometry, with local refinement around the cell embedded in the gel. The blowup shows details of the mesh inside and around the elastic cell.

view. This mesh has 3072 elements and 65,251 degrees of freedom, with the smallest mesh size $h_{min} = 1.42 \times 10^{-3}$. We have confirmed adequate temporal and spatial resolution by refining the mesh and the time step, with the minimum mesh size varying from 2.94×10^{-3} down to 1.33×10^{-3}, and the time step Δt from 10^{-6} down to 10^{-8}. All the variables of interest vary within 0.2%, with the maximum interstitial velocity v_{fx} varying by 0.066%, and the maximum interfacial displacement u_{sx} by 0.036%. The results reported below are based on the mesh of Fig. 2 with $h_{min} = 1.42 \times 10^{-3}$ and time step $\Delta t = 5 \times 10^{-8}$. Similar tests have been done to ensure accurate resolutions in the normal-flow geometry.

3 Results: shear-flow geometry

We first report the model predictions in the shear geometry. Unless explicitly stated otherwise, all results are at steady state.

3.1 Gel without embedded cell

To study the interstitial flow in the gel chamber that is entrained by the perfusion, we first simulate the case without an embedded cell. Figure 3 shows the flow and pressure fields in the gel. In the perfusion channel upstream of

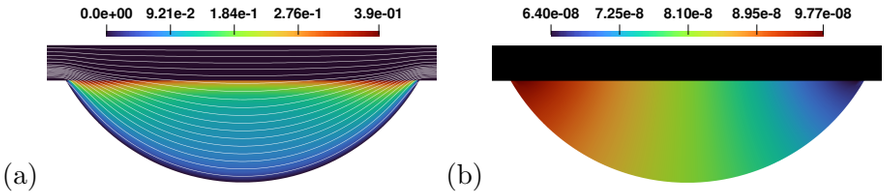

Figure 3: Interstitial flow inside the gel chamber. (a) Streamlines and the magnitude of the velocity shown by color contours. The velocity magnitude has been scaled by $V_0 = 3$ μm/s, and the maximum dimensional magnitude is 1.17 μm/s. (b) Pressure contours in the gel chamber. The magnitude of the pressure has been scaled by $\mu_s = 40$ kPa (see Appendix B for dimensional parameter values.)

the gel chamber, the fluid obeys no slip BC on the solid wall. Upon contact with the surface of the gel, however, the fluid entrains a shear flow inside the gel. Meanwhile, the pressure gradient in the clear-fluid channel acts to inject fluid into the gel in the upstream portion of the interface Γ_1, and draws it out in the downstream portion. The magnitude of the interstitial flow, on the order of 1 μm/s, is consistent with flows in the Disse space of the liver sinusoid *in vivo* [51] and in sinusoid-on-chip devices [52, 53]. The flow in the gel can be roughly divided into three regions. Immediately below the interface Γ_1, the flow is entrained by the shear outside, via the boundary conditions. In the bulk of the gel, the interstitial flow is mostly driven by the pressure gradient. Further below is a wall region where the Brinkman shear stress is again prominent. In comparison with the interfacial and wall regions, the intermediate Darcy region features a relatively uniform velocity, with a small shear rate.

To examine how the perfusion affects the hydrogel domain, Fig. 4 plots profiles of the velocity and gel displacement components along the interface Γ_1. The vertical component v_{fy} of Fig. 4(b) confirms the injection and ejection in the upstream and downstream half of the interface. The injection removes the perfusate from the channel, whereas the ejection returns it. As a result, the longitudinal velocity in the channel has a local minimum in the middle of the domain ($X = 2$), and so does the entrained flow v_{fx} of Fig. 4(a). The horizontal flow pushes the gel downstream on the interface ($u_{sx} > 0$), with the greatest displacement at the center $X = 2$ (Fig. 4c). The injection in the upstream portion depresses the interface ($u_{sy} < 0$) while the ejection raises it in the downstream portion ($u_{sy} > 0$) (Fig. 4d). Given the relatively large gel moduli and the small capillary number Ca (Table 1), the

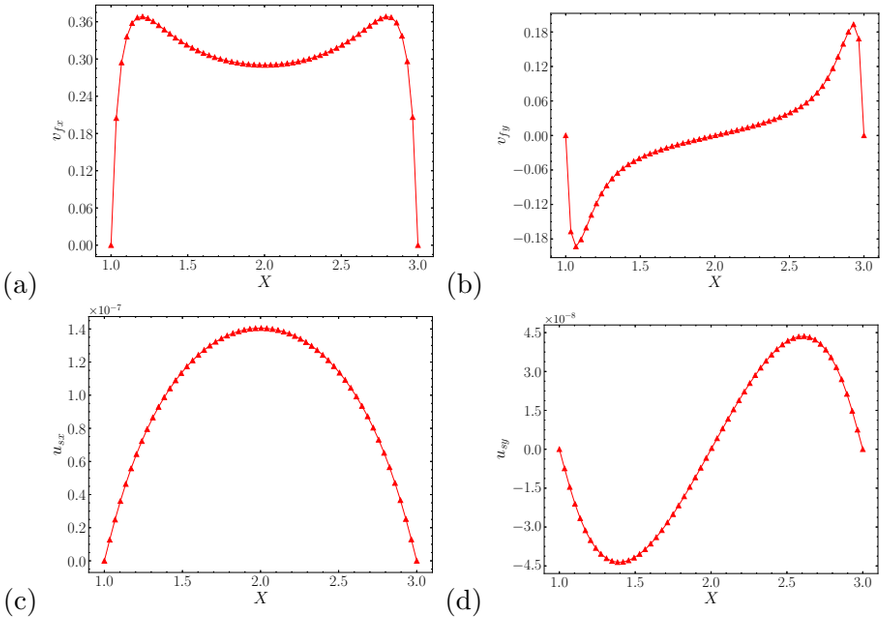

Figure 4: Interfacial profiles of the velocity components (a) v_{fx} and (b) v_{fy} along the gel surface Γ_1, and the gel displacement components (c) u_{sx} and (d) u_{sy}. Since the gel deforms under the flow, we use the Lagrangian coordinate X (corresponding to the undeformed interface) as the abscissa.

gel deformation is minimal. Thus, the profiles show an approximate fore-aft symmetry or anti-symmetry.

The interstitial flow deforms the solid network in the gel, and engenders solid displacement, strain and stress. The displacement is larger away from the solid boundary (Fig. 5a); it is largest in the mid-section of the chamber close to the interface Γ_1. The strain and stress, on the other hand, are largest near the solid boundary and away from the gel surface. This is illustrated by the distribution of the von Mises stress based on the solid stress $\boldsymbol{\sigma}_s$ in Fig. 5(b). Thus, the gel is most stressed at the two corners of the gel chamber. There, the proximity between the deformable gel surface Γ_1 and the solid bowl below it implies large elastic strains. In contrast, the gel in the middle of the chamber and farthest from the solid boundary experiences the lowest stress; it is mostly displaced slightly downstream. Because the solid displacement is small, the solid volume fraction ϕ_s hardly deviates from its undeformed value of $\phi_0 = 0.01$ anywhere in the gel domain.

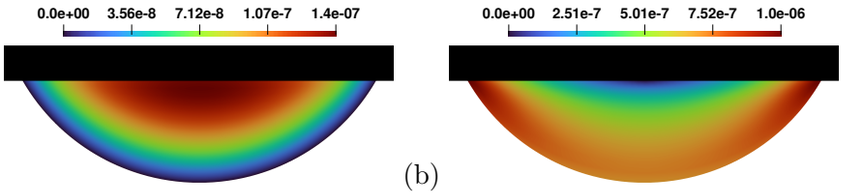

Figure 5: (a) The magnitude of the solid displacement $|\mathbf{u}_s|$ inside the gel chamber. (b) The von Mises stress σ_{sv} based on the solid stress $\boldsymbol{\sigma}_s$ (Eq. 8).

3.2 Gel with embedded cell

We embed a cell of diameter $d = 0.06$ at $e = 0.2$ below the interface along the midline of the gel chamber, and repeat the simulation above. The streamlines are disturbed in the neighborhood of the cell, whose surface is impermeable to the fluid (Fig. 6a). Thus, the streamlines resemble those in low-Reynolds number flows of a pure fluid around an obstacle. Similarly, a high-pressure zone prevails upstream of the cell, and a low-pressure zone downstream (Fig. 6b), although this pattern is somewhat obscured by the large-scale pressure gradient in the gel due to the Darcy drag.

To understand the interaction between the cell and its surrounding gel, we first examine how the cell affects the gel. Despite its relatively small size, the cell disturbs the velocity profiles on the fluid-gel interface. By bending the streamlines above it and effectively reducing the flow area there, the cell raises v_{fx} and produces a local maximum very close to the midline ($X = 2$) (Fig. 7a). Meanwhile, it elevates the vertical component v_{fy} upstream of the midline, and depresses it downstream (Fig. 7b). The changes in the interfacial velocity profiles, therefore, is consistent with the streamlines of Fig. 6(a). Via the flow field, the cell also affects the interfacial displacement. Owing to the acceleration of the longitudinal flow v_{fx} upstream, the longitu-

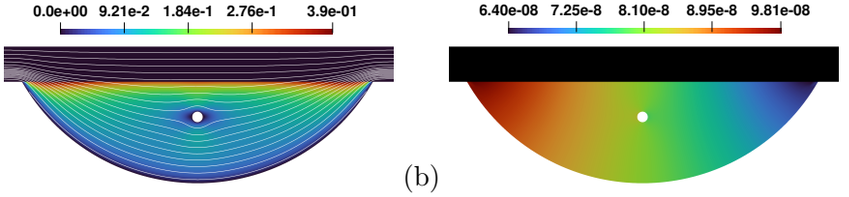

Figure 6: Interstitial flow inside the gel chamber with an embedded cell. (a) Streamlines and the magnitude of the velocity shown by color contours. (b) Pressure contours.

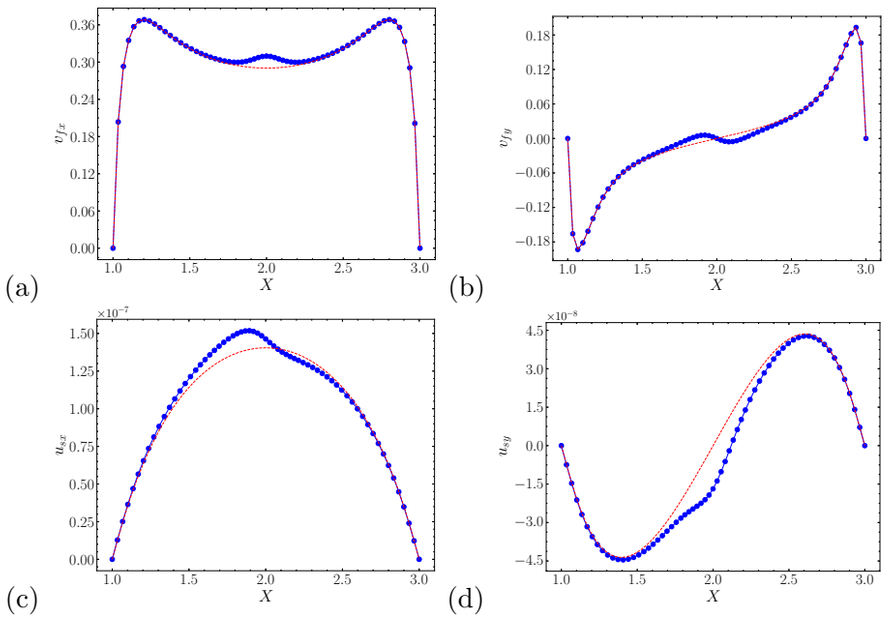

Figure 7: Steady-state profiles along the gel surface Γ_1 with the embedded cell: (a) horizontal fluid velocity component v_{fx}; (b) vertical component v_{fy}; (c) horizontal solid displacement u_{sx}; (d) vertical displacement u_{sy}. For comparison, the red dotted lines indicate the profiles without the cell.

dinal displacement u_{sx} receives a boost upstream of the midpoint (Fig. 7c). The vertical displacement in Fig. 7(d), on the other hand, experiences a depression around the midpoint. This is somewhat surprising in view of the anti-symmetric velocity disturbances of Fig. 7(b).

To rationalize the interfacial depression, we must now consider how the gel affects the cell. Under the influence of the interstitial flow, the cell predominantly moves toward the right, with a small downward movement (Fig. 8a). Meanwhile, the cell undergoes largely uniform compression, as indicated by the displacement vectors relative to the cell's centroid inside and around the cell (Fig. 8b). The von Mises strain inside the cell varies within the narrow range of $1.38 \sim 1.39\times10^{-6}$, and the von Mises stress in the range of $5.43 \sim 5.47\times10^{-8}$. The rightward movement of the cell would cause the gel surface to fall in the upstream region and rise in the downstream region. However, the shrinkage of the cell eliminates the downstream rise, and explains the interfacial depression in Fig. 7(d). In fact, the compression of the cell accounts for about 96% of the volume shrinkage below Γ_1. Only

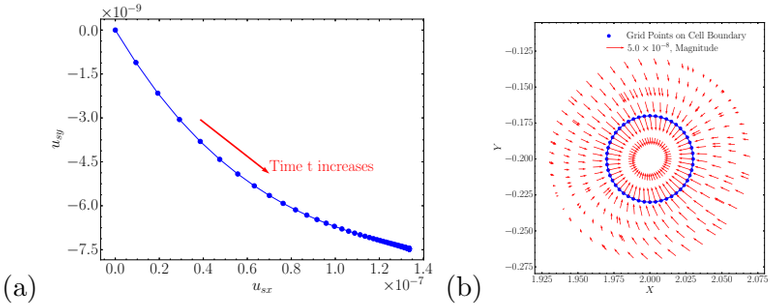

Figure 8: (a) Trajectory of the cell's centroid as it moves under the interstitial flow. Note the smaller scale used for u_{sy}. (b) Steady-state displacement vectors relative to the cell centroid inside the cell and in the surrounding gel. The blue line and dots mark the cell boundary. For better visibility, we plot only vectors on selected vertices inside and outside the cell.

about 4% is due to the compression of the gel itself. As a result, the solid fraction ϕ_s remains mostly at its undeformed level.

The cell is subject to the following stresses from the surrounding gel: the pressure, the Brinkman stress of the interstitial fluid and the stress of the solid network in the gel. Thus, the total traction on the cell surface is $\mathbf{n} \cdot (\phi_f \boldsymbol{\sigma}_f + \phi_s \boldsymbol{\sigma}_s - p\mathbf{I})$. Figure 9 shows spatial contours of the magnitudes of the three components and their sum. Among the three, p is the largest in magnitude, albeit with relatively minor variations around the cell, and the Brinkman stress $\phi_f \boldsymbol{\sigma}_f$ is the smallest. In fact, a scaling argument suggests that the Brinkman stress is negligible relative to the Darcy drag in most cases [54, 55].

From Figs. 8 and 9, we extract the following understanding about the mechanical coupling between the gel and the cell. First, pressure p is the driving force for the coupling. It produces the Darcy flow in the gel, as well as the main thrust for cell movement and deformation. Second, we can conceptually divide the effect of p on the cell into two parts, one due to the averaged p, and the other due to the p variation across the cell. The former produces an isotropic compression of the cell, as depicted in Fig. 8(b), while the latter the cell movement in Fig. 8(a). Third, the gel deforms owing to two factors, the Darcy flow and the cell movement. Thus, the elastic stress $\boldsymbol{\sigma}_s$ arises in the gel as the result of how the cell boundary displaces the gel relative to how the gel would have moved in the cell-free situation of Sec. 3.1. In particular, the cell shrinkage of Fig. 8(b) stretches the surrounding gel radially and produces radial tensile stresses visible in Fig. 9(c). The small

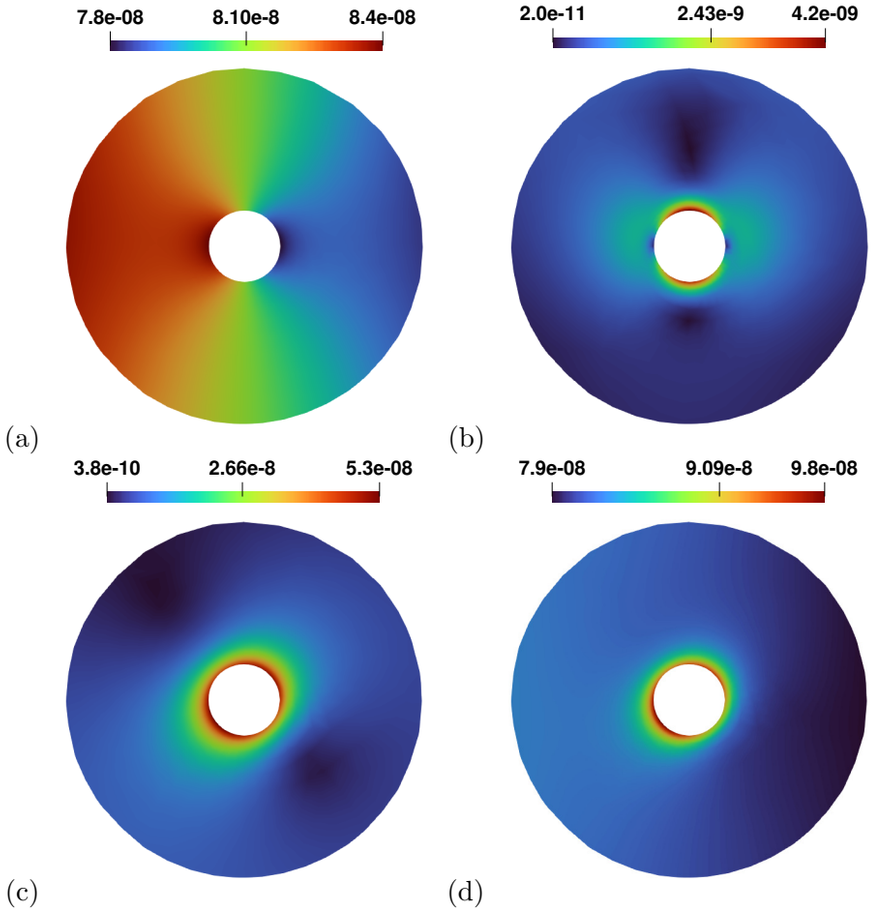

Figure 9: (a) A close-up of the steady-state pressure field surrounding the cell, with a high-pressure region upstream of the cell and a low pressure region downstream. (b) The von Mises stress computed from the fluid stress contribution $\phi_f \boldsymbol{\sigma}_f$. (c) The von Mises stress computed from the solid stress contribution $\phi_s \boldsymbol{\sigma}_s$. (d) The von Mises stress computed from the total stress $\phi_f \boldsymbol{\sigma}_f + \phi_s \boldsymbol{\sigma}_s - p\mathbf{I}$.

anisotropy in Fig. 8(b), with stronger compression in the second and fourth quadrants, is a signature of the shear flow, which is itself manifested by the pattern of the Brinkman stress in Fig. 9(b).

What are the potential biological consequences of the strain and stress suffered by the cell? The maximum total von Mises stress of Fig. 9(d) of

9.80×10^{-8} translates to a dimensional stress of about 3.92 mPa (see Appendix B for baseline moduli). The maximum von Mises strain sustained by the cell is 1.39×10^{-6}. Despite their apparently small magnitude, such stress and strain may produce significant biological effects on the cell. For example, stresses on the order of mPa can promote proliferation of endothelial cells [56], cytoskeleton reorganization and cell-cell adhesion in epithelial cells, osteogenic differentiation of stem cells [57], and apoptosis and metastasis of cancer cells [58]. Intestinal epithelium is known to respond to even smaller stresses in terms of mucus production and microvilli formation [24]. Recent experiments show that shear stress on the mPa scale can induce albumin and growth factor production in liver-on-chip devices [52]. In particular, the optimal stress for stimulating hepatocyte proliferation is found to be around 5 mPa [53]. To damage biological cells in vitro, tens of pascals are required for suspended cells [59, 60], and a shear strain of 15% is required for cells embedded in gels [27]. For the baseline parameters of Table 1, therefore, the flow does not cause any danger to the embedded cell.

But one wonders if faster flow will change this, and how much faster the flow can be without endangering the cell. To probe such questions, we keep all other dimensional parameters fixed and vary the perfusion speed V_0 from the baseline of 3 μm/s up to 100 μm/s. The only dimensionless group affected is Ca, which increases from 3×10^{-10} to 10^{-8}. Because the gel and cell strains remain small, their elastic response is essentially linear. The traction that the cell suffers from the surrounding gel and the cell deformation both increase linearly with Ca. For $Ca = 10^{-8}$, the maximum von Mises stress that the gel exerts on the cell reaches 131 mPa, and the maximum von Mises strain in the cell is 4.62×10^{-5}. These are still orders of magnitude below the critical levels that may cause mechanical damage to the cell [27,59,60]. To produce tens of pascals of external stress, the velocity would need to increase by another two orders of magnitude.

We have also explored the effects of the cell and gel stiffness. Keeping all other parameters fixed, we vary the cell moduli $\mu_c = \lambda_c$ down to 0.1 and up to 10. As expected, softer cells deform more. The maximum von Mises strain sustained by the cell increases about 2.5 times to 3.48×10^{-6} for the softest cell, and decreases about 7 times to 1.98×10^{-7} for the hardest cell. More cell deformation leads to greater deformation in the gel. For the softest cell, the maximum gel surface depression due to the cell is 2.39 times as large as the baseline case of Fig. 7(d). Finally, we have varied the stiffness of the gel $\mu_s = \lambda_s$ while keeping all the other dimensional parameters fixed. As μ_s is used to scale the stresses, this change amounts to varying $\mu_c = \lambda_c$ and Ca in proportion while keeping all other dimensionless groups fixed. Softer

gel suffers greater deformations under the shear flow, and allows greater displacement of the cell. Reducing the gel stiffness by a factor of 10 leads to an increase in the cell displacement by nearly a factor of 8. Meanwhile, the maximum von Mises strain and stress sustained by the cell both increase by about 43%. Thus, the soft gel exposes the cell to greater movement, deformation and stress. Conversely, raising the gel stiffness by a factor of 10 reduces the cell displacement by 86%, and the cell strain and stress by a factor of 4. Thus, stiffer gels shields and protects the cell from mechanical strain and stress.

4 Results: normal-flow geometry

The normal-flow results are mostly based on the parameters of Table 1. We will only vary the cell position e in certain cases.

4.1 Gel without embedded cell

In the normal flow geometry, the perfusate passes through the gel layer held in place by 4 solid posts. Figure 10 shows the streamlines and velocity magnitude inside the gel domain. The four fixed solid pillars cause repeated narrowing and widening of the gel channel, and acceleration and deceleration of the interstitial flow. Therefore, the fastest fluid flow occurs between opposite pillars. This resembles the flow of a viscous fluid around the posts. Note that the magnitude of interstitial flow in Fig. 10 is representative of

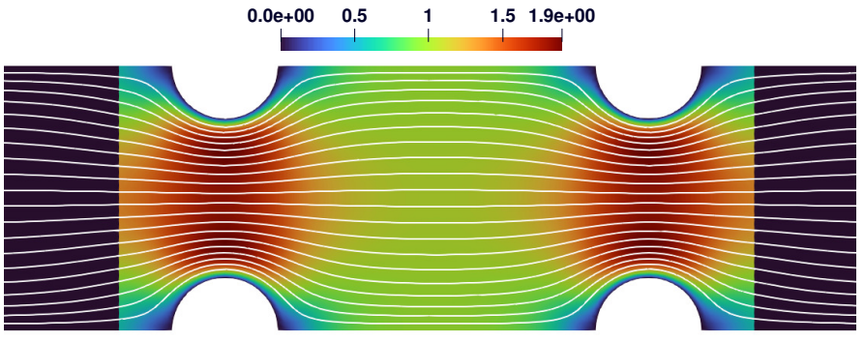

Figure 10: Streamlines and contours of the velocity magnitude for the normal flow through the gel layer. The velocity magnitude has been scaled by $V_0 = 3$ μm/s (see Appendix B), and the maximum magnitude is 5.70 μm/s.

values used *in vitro* [41], and is also consistent with *in vivo* data [15, 61].

As expected, the interstitial flow assumes a much higher velocity than that entrained by the shear flow in Fig. 3, a direct result of the flow kinematics. Accordingly, the normal flow deforms the gel to a much greater extent. For example, the interfaces Γ_1 and Γ_3 both deform in the flow direction, with the maximum displacement at the center being more than 10 times greater than that in the shear-flow geometry (Fig. 4c). The maximum von Mises elastic stress for the solid network, occurring on the solid posts, is about 30 times that of the shear-flow geometry (Fig. 5b).

4.2 Gel with embedded cell

We have placed a single cell in the center of the gel domain ($e = 1.2$ in Fig. 1b), and also at the two constrictions ($e = 0.4$ and 2), to examine how the normal flow in the gel moves and deforms the cell. At the different locations, the cell experiences qualitatively the same influence from the interstitial flow, with different magnitudes. In the following, we mostly present the results with the cell at the center ($e = 1.2$).

The deformation and stress of the gel surrounding the cell turn out to be qualitatively similar to those in the shear-flow geometry, shown in Fig. 8(b) and Fig. 9, albeit at greater magnitudes. The pressure is about 3 times as high in magnitude, and the pressure drop across the cell is about 10 times as large (Fig. 11a). Under such pressure, the cell shrinks almost isotropically (Fig. 11b), at a roughly uniform von Mises strain of 3.84×10^{-6}, nearly 3 times as large as in the shear flow. Accordingly, the gel surrounding the cell experiences largely radial stretching. The pressure gradient pushes the cell downstream, with a steady-state centroid displacement of 2.04×10^{-6}, about 15 times that in the shear flow (Fig. 8a).

Therefore, the gel-cell coupling in the normal flow manifests essentially the same physics as in the shear flow. The pressure is the dominant driver for the gel and cell deformation, and its effect on the cell can be understood from the superposition of two factors: the average magnitude of the pressure compresses the cell, whereas the pressure gradient across the cell pushes it downstream. It is due to the first factor that the cell experiences a largely uniform compression, and also radially stretches the surrounding gel. The second factor breaks the fore-aft symmetry; the gel immediately upstream of the cell suffers a greater tensile strain than that immediately downstream.

For the cell placed in the center of the normal flow ($e = 1.2$), the maximum von Mises strain of 3.84×10^{-6} is still far too small to damage the cell. The maximum von Mises stress exerted by the gel on the cell amounts

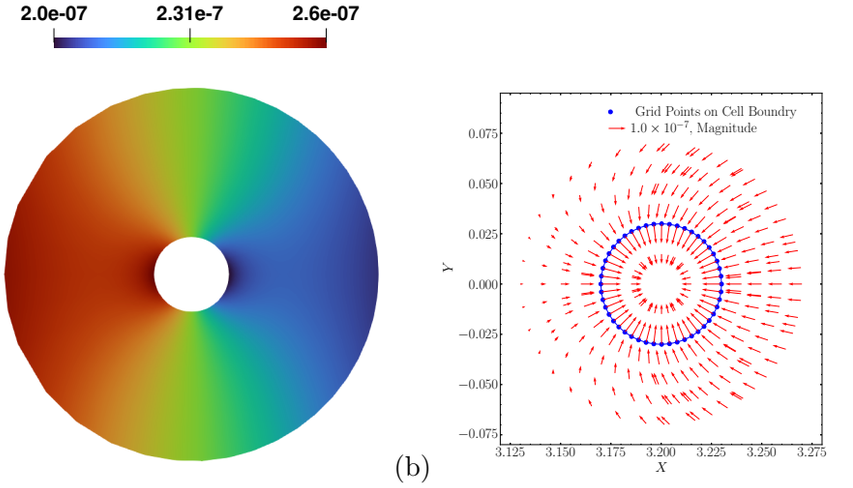

(a) (b)

Figure 11: (a) A close-up of the steady-state pressure field surrounding the cell, with a high-pressure region upstream of the cell and a low pressure region downstream. (b) Displacement vectors relative to the cell centroid, similar to Fig. 8(b). The blue line and dots mark the cell boundary.

to 2.84×10^{-7}, or about 11.3 mPa in dimensional form. Such a stress is too gentle to damage the cell, but large enough to induce significant cell dynamics such as hepatocyte regeneration [52, 53]. When we place the cell in the front or the rear constriction ($e = 0.4$ or 2), the most noticeable difference is the degree of compression suffered by the cell. For the cell at the front, the maximum von Mises strain is 65% greater than at the center, whereas for the cell at the rear, it is 49% lower. This is a direct result of the hydrostatic pressure being higher upstream than downstream.

5 Conclusion

Motivated by the recent advances in microfluidic organ-on-chip devices, this work focuses on the fluid and solid mechanics in such devices. The objectives of this study are two-fold. The first is to build a general theoretical and computational framework for studying the mechanics of a hydrogel under perfusion. The second is to explore the mechanical interaction between the gel and an embedded biological cell under realistic flow conditions. The main contributions of this work can be summarized as follows.

(a) We have presented a poroelastic model that accounts for all the key

mechanisms in a typical cell-in-gel device, including perfusion, permeation of the perfusate into the gel to reach the cell, elastic deformation of the gel and the cell, and mechanical coupling between the gel and the cell.

(b) We have developed a finite-element package for simulating such devices, accounting for the two prototypical geometries dominated respectively by shear flow of the perfusate along the gel surface and by normal flow through a gel layer.

(c) The hydrogel transmits strain and stress from the perfusate-gel interface toward the embedded cell. Softer cells deform more, of course. But stiff gels can protect the cells from severe deformation.

(d) Pressure is the most important stress component in defining the cell deformation and stress. The elastic stress in the gel surrounding the cell is the second most important; it is determined by the relative displacement of the cell surface to the gel, due to cell deformation or movement. The viscous Brinkman stress due to interstitial flow is the least important stress component.

(e) Using realistic parameters for the perfusate, the hydrogel and the cell, our model predicts velocity and stresses in the gel and the cell that are comparable in magnitude with *in vitro* and *in vivo* data. In particular, the cells sustain stresses on the order of a few millipascals, consistent with the level of stress in experimental liver-chips that has been shown to stimulate hepatocyte regeneration.

This work provides a tool for designing hydrogel-based cell cultures in microfluidics, and for predicting the transmission of mechanical forces from the flow of perfusate toward the cells. Thus, it offers a key component in analyzing mechanotranduction in gel-cell systems [62]. The complementary component, the biochemical response of cells to mechanical stimulation [63], is not accounted for in the present work. Embedded cells are also known to actively remodel its surrounding extracellular matrix, degrading it by proteolysis, reinforcing it by depositing proteins, or restructuring and realigning the fibers [64]. Such remodeling can change the porosity, polymer concentration and elastic stiffness of the gel, and introduce spatial inhomogeneity. Our model assumes an initially homogeneous hydrogel, and disregards gel remodeling by the cell. In addition, cells adapt their shape to the microenvironment, e.g., appearing globular or spindle-like depending on the hydrogel

matrix [65]. Such shape change and orientation would surely modify the stress and strain experienced by the cells, effects not accounted for in our current model. Moreover, we have considered only a single isolated cell, whereas cell cultures invariably involve clusters or colonies of cells. The mechanical and biochemical interactions among the neighbors will be another important factor to be studied. Finally, our study is in planar two-dimensional geometries. Many microfluidic devices are thin, with narrowly spaced walls inhibiting out of plane movement. But our main motivation is to save on computational cost in this initial study aimed at exploring the basic physical principles. High-fidelity simulation of specific devices should reflect their three-dimensionality. Given the above limitations of the current work, it should be regarded as a first step toward the goal of understanding the dynamics of cells in hydrogels, as encountered in organoids and artificial tissues *in vitro* [52, 53], as well as during embryogenesis [66] and wound healing [67] *in vivo*.

Acknowledgements. We acknowledge financial support by the Natural Sciences and Engineering Research Council of Canada (Discovery Grant No. 2019-04162, 2024-03982, Alliance International Grant No. 586462-23) for J.J.F., by the National Science Foundation (Grants DMS-2012480, DMS-2309732) for P.Y., and by the Natural Science Foundation of China (Grant No. 12401511), the Guangdong Basic and Applied Basic Research Foundation (Grant No. 2023A1515110861), and Guangdong Provincial Key Laboratory of IRADS (2022B1212010006) for J.Z. We thank Yu Du, Mian Long, Amir Reza Mohebi and Zelai Xu for helpful discussions.

Appendix A Scaling

We choose a characteristic length L_0 and a characteristic velocity V_0 for the geometry of the specific problem. Then the characteristic time is L_0/V_0. Furthermore, we adopt the second Lamé constant μ_s for the hydrogel solid network as a characteristic stress. The following scaling renders the governing equations and boundary conditions dimensionless:

$$(\bar{x}, \bar{y}, \bar{\mathbf{u}}_s, \bar{\mathbf{u}}_c) = (x, y, \mathbf{u}_s, \mathbf{u}_c)/L_0, \quad (\bar{\mathbf{V}}, \bar{\mathbf{v}}_f, \bar{\mathbf{v}}_s, \bar{\mathbf{v}}_c) = (\mathbf{V}, \mathbf{v}_f, \mathbf{v}_s, \mathbf{v}_c)/V_0,$$
$$\bar{t} = tV_0/L_0, \quad (\bar{\boldsymbol{\Sigma}}, \bar{\boldsymbol{\sigma}}_f, \bar{\boldsymbol{\sigma}}_s, \bar{\boldsymbol{\sigma}}_c, \bar{P}, \bar{p}) = (\boldsymbol{\Sigma}, \boldsymbol{\sigma}_f, \boldsymbol{\sigma}_s, \boldsymbol{\sigma}_c, P, p)/\mu_s,$$

where the bar denotes dimensionless quantities. Certain length ratios are fixed for the entire paper, including $\bar{W} = 0.2$, $\theta = \pi/3$ for the shear flow, $\bar{a} = 0.2$, $\bar{D} = 0.4$ for the normal flow and other ratios indicated in Fig. 1.

The cell diameter $\bar{d} = 0.06$ is fixed in both flow geometries. The position of the cell $\bar{e}$, on the other hand, will be varied and thus included in the dimensionless groups below. Out of the 12 geometric and physical parameters of the problem, $e,\ \mu_s, \lambda_s, \mu_c, \lambda_c, \xi, \mu, L_0, V_0, \eta, \beta, \phi_{s0}$, we define the following 9 dimensionless groups:

$$\bar{e} = e/L_0, \bar{\lambda}_s = \lambda_s/\mu_s, \bar{\lambda}_c = \lambda_c/\mu_s, \bar{\mu}_c = \mu_c/\mu_s,$$
$$\bar{\xi} = \xi L_0^2/\mu, (\bar{\beta}, \bar{\eta}) = (\beta, \eta)\mu/L_0, Ca = V_0\mu/(L_0\mu_s), \phi_{s0},$$

where ϕ_{s0} is the initial solid fraction in the undeformed hydrogel. Ca indicates the ratio between the external viscous stress and the elastic stress of the solid skeleton, and can be viewed as an effective capillary number. Since the results and discussions mostly concern dimensionless variables, we have dropped the overbar in the main text. The dimensionless governing equations are as follows:

$$\frac{\partial \phi_s}{\partial t} + \nabla \cdot (\phi_s \mathbf{v}_s) = 0, \tag{A.1}$$
$$\nabla \cdot (\phi_s \mathbf{v}_s + \phi_f \mathbf{v}_f) = 0, \tag{A.2}$$
$$\nabla \cdot (\phi_f \boldsymbol{\sigma}_f) - \phi_f \nabla p + \xi Ca\, \phi_f \phi_s (\mathbf{v}_s - \mathbf{v}_f) = 0, \tag{A.3}$$
$$\nabla \cdot (\phi_s \boldsymbol{\sigma}_s) - \phi_s \nabla p + \xi Ca\, \phi_f \phi_s (\mathbf{v}_f - \mathbf{v}_s) = 0, \tag{A.4}$$
$$\frac{d\mathbf{u}_s}{dt} - \mathbf{v}_s = 0, \tag{A.5}$$
$$\nabla \cdot \mathbf{V} = 0, \tag{A.6}$$
$$\nabla \cdot \boldsymbol{\Sigma} - \nabla P = 0, \tag{A.7}$$
$$\nabla \cdot \boldsymbol{\sigma}_c = 0, \tag{A.8}$$
$$\boldsymbol{\sigma}_f = Ca(\nabla \mathbf{v}_f + \nabla \mathbf{v}_f^T), \tag{A.9}$$
$$\boldsymbol{\sigma}_s = J^{-1}(\mathbf{F} \cdot \mathbf{F}^T - \mathbf{I}) + \lambda_s (J-1)\mathbf{I}, \tag{A.10}$$
$$\boldsymbol{\Sigma} = Ca(\nabla \mathbf{V} + \nabla \mathbf{V}^T). \tag{A.11}$$

The dimensionless boundary conditions appear the same as the dimensional ones given in Section 2.3, except for the following three on the gel-fluid interface:

$$Ca\,(\mathbf{V} - \mathbf{v}_f) \cdot \mathbf{n} = \eta\, \mathbf{n} \cdot [(\boldsymbol{\Sigma} - P\mathbf{I}) - (\boldsymbol{\sigma}_s - p\mathbf{I})] \cdot \mathbf{n}, \tag{A.12}$$
$$Ca\,(\mathbf{V} - \mathbf{v}_f) \cdot \mathbf{t} = \beta\,(\boldsymbol{\Sigma} \cdot \mathbf{n}) \cdot \mathbf{t}, \tag{A.13}$$
$$Ca\,\phi_s(\mathbf{v}_s - \mathbf{v}_f) \cdot \mathbf{t} = -\beta\,(\boldsymbol{\sigma}_s \cdot \mathbf{n}) \cdot \mathbf{t}. \tag{A.14}$$

Appendix B Parameter estimation

In presenting results in the main text, we have omitted the overbar for dimensionless groups since the discussion rarely concerns dimensional parameters. In this appendix, however, both types are present. Thus, we revert temporarily to using an overbar to distinguish a dimensionless parameter from its dimensional counterpart.

Initial solid fraction: Many hydrogels have high porosity, with a swelling ratio reaching 40 or higher (corresponding to solid fraction of 2.5% or lower) [68]. We have taken the initial solid fraction $\phi_{s0} = 0.01$ for an initial 99% porosity [69].

Elastic moduli: Hydrogels can have a wide range of stiffness, with Young's modulus E ranging from hundreds of pascals to tens of kPa [44]. Poisson's ratio ν has been reported to be between 0.2 and 0.33 [70, 71]. For simplicity, we choose $\nu = 0.25$ such that the two Lamé constants are equal (see Eq. 7). However, the experiments measured the response of the entire hydrogel, including both the solid and the liquid. In the notation of our BC (Eq. 14), they measured $P - p = \phi_s \sigma_s$. Thus, a measured $E_m = 10^3$ Pa translates to $E = E_m/\phi_s = 10^5$ Pa in our constitutive equation (Eqs. 6, 7). This further translates to $\lambda_s = \mu_s = 4 \times 10^4$ Pa.

Biological cells also exhibit a wide range of stiffness; Luo *et al.* [43] cited E values from hundreds to thousands of pascals. These values are largely comparable to those of hydrogels; in fact, an advantage of adopting hydrogels in cell cultures is the ability to tune their stiffness to match that of the cells. For simplicity, therefore, we have taken $\mu_c = \lambda_c = \mu_s = \lambda_s$. This implies Poisson's ratio $\nu = 0.25$ for the cell as well, with a compressibility comparable to chondrocytes [72]. Thus, we have the following baseline values for the dimensionless groups: $\bar{\lambda}_s = \bar{\lambda}_c = \bar{\mu}_c = 1$.

Darcy drag coefficient: ξ appears in the momentum equation, which, if written in the traditional Darcy's law or Brinkman's form, involves the bulk permeability k. Comparing these two forms establishes the following connection:

$$\xi = \frac{\mu}{k} \frac{\phi_f}{\phi_s}, \tag{B.1}$$

so that ξ can be evaluated from the more familiar parameter k. In particular, we adopt the Darcy permeability formula suitable for high-porosity media [36, 73]:

$$k = \frac{2r^2}{9} \frac{\phi_f}{\phi_s}, \tag{B.2}$$

where r is a characteristic pore radius, which falls in the wide range of 0.1–100 μm for hydrogels [74–76]. Thus, $\xi = 4.5\mu/r^2$. Taking $\mu = 10^{-3}$ Pa·s for water, and $r = 2.5$ μm as a typical pore size, we get $\xi = 7.2 \times 10^8$ kg/(m^3·s). The dimensionless group $\bar{\xi} = \xi L_0^2/\mu = 4.5(L_0/r)^2$ is directly related to the pore-to-sample size ratio. The macroscopic size of the devices ranges from hundreds of microns to millimeters [41, 42]. Taking $r = 2.5$ μm and $L_0 = 250$ μm, we get $\bar{\xi} = 4.5 \times 10^4$.

Interfacial permeability and slip coefficients: Our boundary conditions introduce the interfacial permeability η via Eq. (15), which can be rewritten as

$$\mu \frac{(\mathbf{V} - \mathbf{v}_f) \cdot \mathbf{n}}{\mu\eta} = \mathbf{n} \cdot [(\boldsymbol{\Sigma} - P\mathbf{I}) - (\boldsymbol{\sigma}_s - p\mathbf{I})] \cdot \mathbf{n}, \tag{B.3}$$

which gives the quantity $\mu\eta$ the meaning of a "penetration length", i.e., the depth into the gel over which the fluid's normal velocity changes from $\mathbf{V}$ to $\mathbf{v}_f$. This idea has recently been explored in a pore-scale model [40], which shows that for hydrogels, this penetration length ranges from r to $4r$. Taking an intermediate value of $2r$, we get the dimensionless $\bar{\eta} = \mu\eta/L_0 = 2r/L_0 = 0.02$ for $r = 2.5$ μm, $L_0 = 250$ μm.

Similarly, the dimensionless slip coefficient $\bar{\beta} = \mu\beta/L_0$ can be seen as the slip length divided by the macroscopic length scale. Prior calculations showed that shear flow past the surface of a porous medium entrains the interstitial fluid down to a depth on the order of $2r$ [77]. This yields $\bar{\beta} = 0.02$.

Capillary number: In the shear-flow geometry, Bachmann *et al.* [42] adopted a tangential velocity $V_0 = 3$ μm/s. In the normal-flow geometry, Polacheck *et al.* [41] tested interstitial velocities $v_f = 0.3$ μm/s and 3 μm/s. In our computations, we have taken $V_0 = 3$ μm/s as a representative velocity for both flow geometries. With $L_0 = 250$ μm, $\mu = 10^{-3}$ Pa·s, and $\mu_s = 4 \times 10^4$ Pa, we obtain $Ca = \mu V_0/(\mu_s L_0) = 3 \times 10^{-10}$ for both the shear- and normal-flow geometries.

Based on the above, we tabulate the baseline values for the dimensionless parameters in Table 1.

Dimensionless groups	Shear flow	Normal flow
$\bar{e}$	0.2	1.2
ϕ_{s_0}	0.01	0.01
$\bar{\lambda}_s$	1	1
$\bar{\lambda}_c$	1	1
$\bar{\mu}_c$	1	1
$\bar{\xi}$	4.5×10^4	4.5×10^4
$\bar{\beta}$	0.02	0.02
$\bar{\eta}$	0.02	0.02
Ca	3×10^{-10}	3×10^{-10}

Table 1: Baseline values for the dimensionless parameters used in the shear-flow and normal-flow simulations.

References

[1] T.-C. Ho, C.-C. Chang, H.-P. Chan, T.-W. Chung, C.-W. Shu, K.-P. Chuang, T.-H. Duh, M.-H. Yang, Y.-C. Tyan, Hydrogels: Properties and applications in biomedicine, Molecules 27 (9) (2022) 2902.

[2] M. W. Tibbitt, K. S. Anseth, Hydrogels as extracellular matrix mimics for 3D cell culture, Biotechnol. Bioeng. 103 (4) (2009) 655–663.

[3] J. S. Jeon, S. Bersini, M. Gilardi, G. Dubini, J. L. Charest, M. Moretti, R. D. Kamm, Human 3D vascularized organotypic microfluidic assays to study breast cancer cell extravasation, Proc. Natl. Acad. Sci. U.S.A. 112 (1) (2015) 214–219.

[4] V. van Duinen, S. J. Trietsch, J. Joore, P. Vulto, T. Hankemeier, Microfluidic 3D cell culture: from tools to tissue models, Curr. Opin. Biotechnol. 35 (2015) 118–126.

[5] H. Liu, Y. Wang, K. Cui, Y. Guo, X. Zhang, J. Qin, Advances in hydrogels in organoids and organs-on-a-chip, Adv. Mater. 31 (50) (2019) 1902042.

[6] N. Dadgar, A. M. Gonzalez-Suarez, P. Fattahi, X. Hou, J. S. Weroha, A. Gaspar-Maia, G. Stybayeva, A. Revzin, A microfluidic platform for cultivating ovarian cancer spheroids and testing their responses to chemotherapies, Microsyst. Nanoeng. 6 (1) (2020) 93.

[7] O. Habanjar, M. Diab-Assaf, F. Caldefie-Chezet, L. Delort, 3D cell culture systems: tumor application, advantages, and disadvantages, Int. J. Mol. Sci. 22 (22) (2021) 12200.

[8] A. Clancy, D. Chen, J. Bruns, J. Nadella, S. Stealey, Y. Zhang, A. Timperman, S. P. Zustiak, Hydrogel-based microfluidic device with multiplexed 3D in vitro cell culture, Sci. Rep. 12 (1) (2022) 17781.

[9] G. Choe, J. Park, H. Park, J. Y. Lee, Hydrogel biomaterials for stem cell microencapsulation, Polymers 10 (9) (2018) 997.

[10] S. Trombino, C. Servidio, F. Curcio, R. Cassano, Strategies for hyaluronic acid-based hydrogel design in drug delivery, Pharmaceutics 11 (8) (2019) 407.

[11] C. A. Dreiss, Hydrogel design strategies for drug delivery, Curr. Opin. Colloid Interface Sci. 48 (2020) 1–17.

[12] S.-M. Kang, J.-H. Lee, Y. S. Huh, S. Takayama, Alginate microencapsulation for three-dimensional in vitro cell culture, ACS Biomater. Sci. Eng. 7 (7) (2020) 2864–2879.

[13] P. Fattahi, A. Rahimian, M. Q. Slama, K. Gwon, A. M. Gonzalez-Suarez, J. Wolf, H. Baskaran, C. D. Duffy, G. Stybayeva, Q. P. Peterson, et al., Core–shell hydrogel microcapsules enable formation of human pluripotent stem cell spheroids and their cultivation in a stirred bioreactor, Sci. Rep. 11 (1) (2021) 7177.

[14] A. Löwa, J. J. Feng, S. Hedtrich, Human disease models in drug development, Nat. Rev. Bioeng. 1 (2023) 545–559.

[15] C.-H. Heldin, K. Rubin, K. Pietras, A. Östman, High interstitial fluid pressure – an obstacle in cancer therapy, Nat. Rev. Cancer 4 (10) (2004) 806–813.

[16] M. A. Swartz, M. E. Fleury, Interstitial flow and its effects in soft tissues, Annu. Rev. Biomed. Eng. 9 (2007) 229–256.

[17] Y. Shou, X. Y. Teo, K. Z. Wu, B. Bai, A. R. K. Kumar, J. Low, Z. Le, A. Tay, Dynamic stimulations with bioengineered extracellular matrix-mimicking hydrogels for mechano cell reprogramming and therapy, Adv. Sci. 10 (21) (2023) 2300670.

[18] C. T. Mierke, Extracellular matrix cues regulate mechanosensing and mechanotransduction of cancer cells, Cells 13 (2024) 96.

[19] S.-F. Chang, C. A. Chang, D.-Y. Lee, P.-L. Lee, Y.-M. Yeh, C.-R. Yeh, C.-K. Cheng, S. Chien, J.-J. Chiu, Tumor cell cycle arrest induced by shear stress: Roles of integrins and Smad, Proc. Natl. Acad. Sci. U.S.A. 105 (10) (2008) 3927–3932.

[20] O. Chaudhuri, Viscoelastic hydrogels for 3D cell culture, Biomater. Sci. 5 (8) (2017) 1480–1490.

[21] S. G. Mina, P. Huang, B. T. Murray, G. J. Mahler, The role of shear stress and altered tissue properties on endothelial to mesenchymal transformation and tumor-endothelial cell interaction, Biomicrofluidics 11 (4) (2017) 044104.

[22] C. M. Novak, E. N. Horst, C. C. Taylor, C. Z. Liu, G. Mehta, Fluid shear stress stimulates breast cancer cells to display invasive and chemoresistant phenotypes while upregulating PLAU in a 3D bioreactor, Biotechnol. Bioeng. 116 (11) (2019) 3084–3097.

[23] E. Akbari, G. B. Spychalski, K. K. Rangharajan, S. Prakash, J. W. Song, Competing fluid forces control endothelial sprouting in a 3-D microfluidic vessel bifurcation model, Micromachines 10 (7) (2019) 451.

[24] L. C. Delon, Z. Guo, A. Oszmiana, C.-C. Chien, R. Gibson, C. Prestidge, B. Thierry, A systematic investigation of the effect of the fluid shear stress on Caco-2 cells towards the optimization of epithelial organ-on-chip models, Biomaterials 225 (2019) 119521.

[25] J. M. Hope, J. A. Dombroski, R. S. Pereles, M. Lopez-Cavestany, J. D. Greenlee, S. C. Schwager, C. A. Reinhart-King, M. R. King, Fluid shear stress enhances T cell activation through Piezo1, BMC Biol. 20 (1) (2022) 61.

[26] D. Brindley, K. Moorthy, J. H. Lee, C. Mason, H. W. Kim, I. Wall, Bioprocess forces and their impact on cell behavior: implications for bone regeneration therapy, J. Tissue Eng. 2011 (2011) 620247.

[27] F. Friedland, S. Babu, R. Springer, J. Konrad, Y. Herfs, S. Gerlach, J. Gehlen, H.-J. Krause, L. De Laporte, R. Merkel, E. Noetzel, ECM-transmitted shear stress induces apoptotic cell extrusion in early breast gland development, Front. Cell Dev. Biol. 10 (2022) 947430.

[28] R. De Piano, D. Caccavo, A. A. Barba, G. Lamberti, Polyelectrolyte hydrogels in biological systems: Modeling of swelling and deswelling behavior, Chem. Eng. Sci. 279 (2023) 118959.

[29] W. Hong, X. Zhao, J. Zhou, Z. Suo, A theory of coupled diffusion and large deformation in polymeric gels, J. Mech. Phys. Solids 56 (5) (2008) 1779–1793.

[30] A. Lucantonio, P. Nardinocchi, L. Teresi, Transient analysis of swelling-induced large deformations in polymer gels, J. Mech. Phys. Solids 61 (1) (2013) 205–218.

[31] Y. Hu, Z. Suo, Viscoelasticity and poroelasticity in elastomeric gels, Acta Mech. Sol. Sinica 25 (5) (2012) 441–458.

[32] D. Caccavo, G. Lamberti, A. A. Barba, Mechanics and drug release from poroviscoelastic hydrogels: Experiments and modeling, Eur. J. Pharm. Biopharm. 152 (2020) 299–306.

[33] T. Bertrand, J. Peixinho, S. Mukhopadhyay, C. W. MacMinn, Dynamics of swelling and drying in a spherical gel, Phys. Rev. Appl. 6 (2016) 064010.

[34] G. L. Celora, M. G. Hennessy, A. Münch, B. Wagner, S. L. Waters, A kinetic model of a polyelectrolyte gel undergoing phase separation, Journal of the Mechanics and Physics of Solids 160 (2022) 104771.

[35] L. Li, J. Zhang, Z. Xu, Y.-N. Young, J. J. Feng, P. Yue, An arbitrary Lagrangian-Eulerian method for simulating interfacial dynamics between a hydrogel and a fluid, J. Comput. Phys. 451 (2022) 110851.

[36] Z. Xu, P. Yue, J. J. Feng, A theory of hydrogel mechanics that couples swelling and external flow, Soft Matter 20 (2024) 5389–5406.

[37] W. J. Polacheck, R. Li, S. G. M. Uzel, R. D. Kamm, Microfluidic platforms for mechanobiology, Lab Chip 13 (2013) 2252–2267.

[38] J. J. Feng, Y.-N. Young, Boundary conditions at a gel-fluid interface, Phys. Rev. Fluids 5 (12) (2020) 124304.

[39] Z. Xu, J. Zhang, Y.-N. Young, P. Yue, J. J. Feng, A comparison of four boundary conditions for the fluid-hydrogel interface, Phys. Rev. Fluids 7 (2022) 093301.

[40] Z. Xu, P. Yue, J. J. Feng, Estimating the interfacial permeability for flow into a poroelastic medium, Soft Matter 20 (2024) 7357–7361.

[41] W. J. Polacheck, J. L. Charest, R. D. Kamm, Interstitial flow influences direction of tumor cell migration through competing mechanisms, Proc. Natl. Acad. Sci. U.S.A. 108 (27) (2011) 11115–11120.

[42] B. Bachmann, S. Spitz, M. Rothbauer, C. Jordan, M. Purtscher, H. Zirath, P. Schuller, C. Eilenberger, S. F. Ali, S. Mühleder, E. Priglinger, M. Harasek, H. Redl, W. Holnthoner, P. Ertl, Engineering of three-dimensional pre-vascular networks within fibrin hydrogel constructs by microfluidic control over reciprocal cell signaling, Biomicrofluidics 12 (4) (2018) 042216.

[43] Q. Luo, D. Kuang, B. Zhang, G. Song, Cell stiffness determined by atomic force microscopy and its correlation with cell motility, Biochim. Biophys. Acta, Gen. Subj. 1860 (9) (2016) 1953–1960.

[44] D. Lee, H. Zhang, S. Ryu, Elastic modulus measurement of hydrogels, in: M. I. H. Mondal (Ed.), Cellulose-Based Superabsorbent Hydrogels, Springer International Publishing, Cham, 2018, pp. 1–21.

[45] D. Arndt, W. Bangerth, M. Bergbauer, M. Feder, M. Fehling, J. Heinz, T. Heister, L. Heltai, M. Kronbichler, M. Maier, P. Munch, J.-P. Pelteret, B. Turcksin, D. Wells, S. Zampini, The deal.II library, version 9.5, J. Num. Math. 31 (3) (2023) 231–246.

[46] E. Gabriel, G. E. Fagg, G. Bosilca, T. Angskun, J. J. Dongarra, J. M. Squyres, V. Sahay, P. Kambadur, B. Barrett, A. Lumsdaine, R. H. Castain, D. J. Daniel, R. L. Graham, T. S. Woodall, Open MPI: Goals, concept, and design of a next generation MPI implementation, in: Recent Advances in Parallel Virtual Machine and Message Passing Interface: 11th European PVM/MPI Users' Group Meeting Budapest, Hungary, September 19-22, 2004. Proceedings 11, Springer, 2004, pp. 97–104.

[47] T. A. Davis, UMFPACK Version 5.2.0 User Guide, Tech. rep., University of Florida, Gainesvill, FL, USA (2007).

[48] M. A. Heroux, J. M. Willenbring, A new overview of the Trilinos project, Sci. Program. 20 (2) (2012) 83–88.

[49] A. Prokopenko, J. Hu, T. Wiesner, C. Siefert, R. Tuminaro, MueLu User's Guide 1.0 (Trilinos version 11.12), Tech. Rep. SAND2014-18874,

Sandia National Laboratories, Albuquerque, NM 87185 and Livermore, CA 94550, USA (October 2014).

[50] P. R. Amestoy, I. S. Duff, J.-Y. L'Excellent, J. Koster, MUMPS: a general purpose distributed memory sparse solver, in: International Workshop on Applied Parallel Computing, Springer, 2000, pp. 121–130.

[51] O. V. Semenova, V. A. Petrov, T. N. Gerasimenko, A. V. Aleksandrova, O. A. Burmistrova, A. A. Khutornenko, A. I. Osipyants, A. A. Poloznikov, D. A. Sakharov, Effect of circulation parameters on functional status of HepaRG spheroids cultured in microbioreactor, Bull. Exp. Biol. Med. 161 (2016) 425–429.

[52] Y. Du, N. Li, H. Yang, C. Luo, Y. Gong, C. Tong, Y. Gao, S. Lü, M. Long, Mimicking liver sinusoidal structures and functions using a 3d-configured microfluidic chip, Lab Chip 17 (2017) 782–794.

[53] W. Li, Y. Wu, W. Hu, J. Zhou, X. Shu, X. Zhang, Z. Zhang, H. Wu, Y. Du, D. Lü, S. Lü, N. Li, M. Long, Direct mechanical exposure initiates hepatocyte proliferation, JHEP Rep. 5 (2023) 100905.

[54] S. Haber, R. Mauri, Boundary conditions for Darcy's flow through porous media, Int. J. Multiphase Flow 9 (1983) 561–574.

[55] O. Coussy, Poromechanics, John Wiley & Sons, 2004.

[56] J. Y. Park, J. B. White, N. Walker, C.-H. Kuo, W. Cha, M. E. Meyerhoff, S. Takayama, Responses of endothelial cells to extremely slow flows, Biomicrofluidics 5 (2) (2011) 022211.

[57] X. Zhang, S. Zhang, T. Wang, How the mechanical microenvironment of stem cell growth affects their differentiation: a review, Stem Cell Res. Ther. 13 (2022) 415.

[58] J. A. Espina, M. H. Cordeiro, M. Milivojevic, I. Pajić-Lijaković, E. H. Barriga, Response of cells and tissues to shear stress, J. Cell Sci. 136 (18) (2023) jcs260985.

[59] M. H. Rahman, Q. Xiao, S. Zhao, F. Qu, C. Chang, A.-C. Wei, Y.-P. Ho, Demarcating the membrane damage for the extraction of functional mitochondria, Microsys. Nanoeng. 4 (2018) 39.

[60] C. H. H. Chan, M. J. Simmonds, K. H. Fraser, K. Igarashi, K. K. Ki, T. Murashige, M. T. Joseph, J. F. Fraser, G. D. Tansley, N. Watanabe,

Discrete responses of erythrocytes, platelets, and von willebrand factor to shear, J. Biomech. 130 (2022) 110898.

[61] H. Dafni, T. Israely, Z. M. Bhujwalla, L. E. Benjamin, M. Neeman, Overexpression of vascular endothelial growth factor 165 drives peritumor interstitial convection and induces lymphatic drain: Magnetic resonance imaging, confocal microscopy, and histological tracking of triple-labeled albumin, Cancer Res. 62 (2002) 6731–6739.

[62] Y. Zhang, P. Habibovic, Delivering mechanical stimulation to cells: State of the art in materials and devices design, Adv. Mater. 34 (32) (2022) 2110267.

[63] P. A. Janmey, C. A. McCulloch, Cell mechanics: integrating cell responses to mechanical stimuli, Annu. Rev. Biomed. Eng. 9 (2007) 1–34.

[64] P. Lu, K. Takai, V. M. Weaver, Z. Werb, Extracellular matrix degradation and remodeling in development and disease, Cold Spring Harb. Perspect. Biol. 3 (12) (2011) a005058.

[65] M. Franchi, Z. Piperigkou, N. S. Mastronikolis, N. Karamanos, Extracellular matrix biomechanical roles and adaptation in health and disease, FEBS J. 291 (3) (2024) 430–440.

[66] D. N. Alasaadi, R. Mayor, Mechanically guided cell fate determination in early development, Cell. Mol. Life Sci. 81 (2024) 242.

[67] R. Agha, R. Ogawa, G. Pietramaggiori, D. P. Orgill, A review of the role of mechanical forces in cutaneous wound healing, J. Surg. Res. 171 (2) (2011) 700–708.

[68] N. Annabi, J. W. Nichol, X. Zhong, C. Ji, S. Koshy, A. Khademhosseini, F. Dehghani, Controlling the porosity and microarchitecture of hydrogels for tissue engineering, Tissue Eng. Part B 16 (4) (2010) 371–383.

[69] N. L. Cuccia, S. Pothineni, B. Wu, J. Méndez Harper, J. C. Burton, Pore-size dependence and slow relaxation of hydrogel friction on smooth surfaces, Proc. Natl. Acad. Sci. U.S.A. 117 (21) (2020) 11247–11256.

[70] J. Yoon, S. Cai, Z. Suo, R. C. Hayward, Poroelastic swelling kinetics of thin hydrogel layers: comparison of theory and experiment, Soft Matter 6 (23) (2010) 6004.

[71] Y.-N. Young, Y. Mori, M. J. Miksis, Slightly deformable Darcy drop in linear flows, Phys. Rev. Fluids 4 (2019) 063601.

[72] W. R. Trickeya, F. P. T. Baaijens, T. A. Laursen, L. G. Alexopoulos, F. Guilak, Determination of the Poisson's ratio of the cell: recovery properties of chondrocytes after release from complete micropipette aspiration, J. Biomech. 39 (2006) 78–87.

[73] Z. Xu, P. Yue, J. J. Feng, Hystereses in flow-induced compression of a poroelastic hydrogel, Soft Matter 20 (2024) 6940–6951.

[74] Y.-C. Chiu, M.-H. Cheng, H. Engel, S.-W. Kao, J. C. Larson, S. Gupta, E. M. Brey, The role of pore size on vascularization and tissue remodeling in PEG hydrogels, Biomaterials 32 (26) (2011) 6045–6051.

[75] A. Salerno, R. Borzacchiello, P. A. Netti, Pore structure and swelling behavior of porous hydrogels prepared via a thermal reverse-casting technique, J. Appl. Polym. Sci. 122 (2011) 3651–3660.

[76] S. Sornkamnerd, M. K. Okajima, T. Kaneko, Tough and porous hydrogels prepared by simple lyophilization of LC gels, ACS Omega 2 (8) (2017) 5304–5314.

[77] D. F. James, A. M. Davis, Flow at the interface of a model fibrous porous medium, J. Fluid Mech. 426 (2001) 47–72.